Coherent range-dependent map-drift algorithm for improving SAR motion compensation

ZHANG Man [1], WANG Guanyong [2,*], WEI Feiming [3,4], and JIN Xue [5]

1. School of Electronic and Communication Engineering, Guangzhou University, Guangzhou 510006, China; 2. Beijing Institute of Radio Measurement, Beijing 100854, China; 3. School of Electronic Information and Electrical Engineering, Shanghai Jiao Tong University, Shanghai 200030, China; 4. No.802 Research Institute of Shanghai Academy of Spaceflight Technology, Shanghai 200050, China; 5. Beijing Institute of Tracking and Communication Technology, Beijing 100094, China

Abstract: Synthetic aperture radar (SAR) is usually sensitive to trajectory deviations that cause serious motion error in the recorded data. In this paper, a coherent range-dependent map-drift (CRDMD) algorithm is developed to accommodate the range-variant motion errors. By utilizing the algorithm as an estimate core, robust motion compensation strategy is proposed for unmanned aerial vehicle (UAV) SAR imagery. CRDMD outperforms the conventional map-drift algorithms in both accuracy and efficiency. Real data experiments show that the proposed approach is appropriate for precise motion compensation for UAV SAR.

Keywords: synthetic aperture radar (SAR), motion compensation (MOCO), coherent map-drift (CMD), range-variant.

1. Introduction

Motion error is a main problematic component that needs to be compensated in airborne synthetic aperture radar (SAR) [1,2] imagery. Motion compensation (MOCO) [3−5] based on high-precision inertial navigation system (INS) measurements is a robust approach to the optimal focal performance. Due to the accuracy limitation of airborne INS, the motion error cannot be measured accurately for unmanned aerial vehicle (UAV) SAR systems [6−9]. Therefore, how to compensate the unknown residual motion error is an inevitable problem for UAV SAR imaging. The autofocus technique [10−13] can effectively estimate the phase error in the data, which is widely used in practical applications. In this paper, an autofocus method is studied to compensate the motion error with higher accuracy and robustness.

For UAV SAR imaging, a series of autofocus methods based on phase gradient autofocus (PGA) [14] and map-drift (MD) [15] have been proposed to estimate the residual phase error after conventional MOCO [16]. The advantage of PGA based algorithm is recognized. It can compensate the phase error with relatively high frequency. However, it has a great demand for strong scattering points in the image, which inevitably reduces the robustness for application. MD estimates the quadratic phase error by the sub-aperture correction, which is more recommended for the advantage of its robustness with the presence of strong noise. For SAR imaging with a wide range and swath [17], the residual range and azimuth-variant phase errors [18−22] affect the imaging quality. These errors are needed to be preciously compensated. A series of space-variant MOCO methods have been developed in recent years to further improve high-resolution airborne SAR imaging [23−27]. In existing work, a range-dependent MD (RDMD) algorithm was proposed [28] for range-variant phase error estimation, and it worked well in real measured data experiment. For RDMD algorithm, the critical principle is similar with the classical MD, that is, it also calculates the correlation function using only the amplitude of sub-aperture data, and then the Doppler rate bias can be theoretically estimated by searching for the peak position of correlation function. However, the amplitude correlation performance between the sub-apertures is usually unspecified or limited in precision. In order to solve this problem, one needs to set long sub-apertures and takes many iteration times to refine the Doppler rate bias estimation in the previous MD works, which inevitably induces great computing and processing complexity. To further improve the estimation accuracy and reduce operational complexity is the motivation of this paper.

In this paper, a coherent RDMD (CRDMD) algorithm is developed. Following existing RDMD algorithm in

[28], CRDMD adapts the coherent correlation [29,30] between sub-apertures to estimate both the constant and linear quadratic phase coefficients with a straight-line integral. The main contribution of the proposed algorithm is given as follows. (i) The sensitivity of phase coherence effectively reduces the convergence times of iterative estimation of phase error, making the algorithm more adaptable to the limited resources of real-time processing. (ii) As the complex-valued coherent correlation function replaces the real-valued amplitude correlation in RDMD, CRDMD provides high accuracy even in the cases of short sub-apertures. CRDMD can accommodate smaller azimuth blocks in the processing, so that higher order phase errors can be estimated compared with RDMD. In addition, RDMD has little restriction on the scene and does not require any special explicit point in the scene, which has higher robustness. In extensive experiments, real UAV SAR data results confirm the accuracy and efficiency improvement by the proposed CRDMD algorithm without robustness loss in dealing with different SAR scenes.

The rest of this paper is organized as follows: Section 2 overviews the RDMD algorithm as was proposed in former studies. Section 3 introduces the proposed CRDMD algorithm in detail. Section 4 presents experimental results with two real measured data sets. Section 5 concludes the paper.

2. Overview of RDMD algorithm

2.1   Signal model

The geometric model of SAR observations is shown in Fig. 1, which is defined in an $O-XYZ$ coordinate. For ideal conditions, the SAR platform moves in a uniform and straight line along the X axis, whose track is shown as the dotted line. In practice, the SAR platform is affected by the unstable air flow, therefore the real flight path has turbulence, which is shown as the solid line.
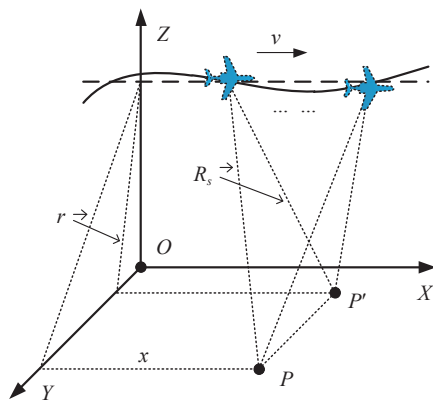

Fig. 1   Geometric model of SAR

In Fig. 1, P and P' are two point targets on the ground, which are located at different cross-track positions. In a synthetic aperture time, the radar echoes reach these two points with different range histories, the echo expression can be uniformly given by

$$s_0(\tau) = W\left(\frac{\tau - \Delta t}{T_p}\right)\cdot$$
$$\exp\left[j2\pi\left(-f_c\Delta t + \frac{\gamma(\tau - \Delta t)^2}{2}\right)\right] \tag{1}$$

where $W(\cdot)$ denotes the window function, τ represents the range time, T_p represents the pulse width, $\Delta t = 2R_s/c$ represents the two-way delay from radar to the point targets, and c is the speed of light. f_c denotes the radar working frequency, and γ represents the signal modulation rate.

After range pulse compression, two-step MOCO [3], and range cell migration correction [31] to (1), the coupling between range and azimuth directions is removed, the signal is expressed as

$$s(t;r) = W\left(\frac{vt - x}{T_a}\right)\cdot\exp\left(-j\frac{4\pi}{\lambda}R_s\right) \tag{2}$$

where

$$R_s = \sqrt{(vt - x)^2 + r^2}. \tag{3}$$

In (2) and (3), t denotes the azimuth time, T_a denotes the aperture duration time, v is the velocity of platform, x denotes the horizontal axis of the point targets, r is the slant range projection, λ denotes the wavelength, and R_s is the instantaneous range between radar and point target P or P'.

Due to the influence of inertial navigation accuracy, residual phase error usually occurs after motion compensation. The echo signal after imaging pre-processing, which contains residual quadratic phase error, is expressed as

$$\tilde{s}(t;r) = s(t;r)\cdot\exp\left(ja_r t^2\right) \tag{4}$$

where a_r represents the residual quadratic phase error coefficient. In this case, autofocus algorithms are necessary for the compensation of the residual phase error. It needs to be emphasized that a_r relies on the slant range projection r. Hence, for point targets P and P', the residual quadratic phase errors are different.

To facilitate the estimation of residual phase error, autofocus algorithms like MD is essential. The standard MD has drawback in real applications on focusing UAV SAR data. For standard MD, the Doppler rate is assumed to be identical at all range bins. It assumes that the quadratic phase error function does not rely on the range bin, and the quadratic phase error is assumed spatial-invariant. However, in real situations involving severe trajectory derivations and wide swath UAV SAR imagery, the range-

dependence of motion errors is never nominal.

2.2 Brief review on RDMD

In order to deal with the problem above, we need to extend the conventional MD to the range-variant model. In this subsection, the principle of RDMD is briefly reviewed based on the previous work in [28]. For a linear range-variant model, the range-variant Doppler rate coefficient a_r in (4) is modeled into a linear function of r as

$$a_r = a + b \cdot r \tag{5}$$

where a is the constant term, and b is the coefficient of one-order term. Following the idea of the standard RDMD, the signal is divided into two sub-apertures, which are given by

$$\tilde{s}_1(t;r) = s\left(t - \frac{T_a}{4};r\right) \cdot$$
$$\exp\left[ja_r\left(t^2 + \frac{T_a^2}{16}\right)\right] \cdot \exp\left(-ja_r\frac{T_a t}{2}\right), \tag{6}$$

$$\tilde{s}_2(t;r) = s\left(t + \frac{T_a}{4};r\right) \cdot$$
$$\exp\left[ja_r\left(t^2 + \frac{T_a^2}{16}\right)\right] \cdot \exp\left(ja_r\frac{T_a t}{2}\right). \tag{7}$$

And the sub-aperture images can be achieved by using an azimuth Fourier transform (FT) to the sub-apertures:

$$\tilde{s}_1(w;r) = \left[\bar{s}_{im}\left(w + \frac{a_r T_a}{2};r\right) \cdot \exp\left(jw\frac{T_a}{4}\right)\right] \otimes h(w), \tag{8}$$

$$\tilde{s}_2(w;r) = \left[\bar{s}_{im}\left(w - \frac{a_r T_a}{2};r\right) \cdot \exp\left(-jw\frac{T_a}{4}\right)\right] \otimes h(w), \tag{9}$$

where $\otimes$ represents the convolution operation, and w represents the azimuth spectrum of sub-aperture data. Functions $\bar{s}_{im}(w;r)$ and $h(w)$ are given by

$$\bar{s}_{im}(w;r) = \int_{-\frac{T_a}{4}}^{\frac{T_a}{4}} s(t;r)\exp(-jwt)\mathrm{d}t, \tag{10}$$

$$h(w) = \int_{-\frac{T_a}{4}}^{\frac{T_a}{4}} \exp\left[ja_r\left(t^2 + \frac{T_a^2}{16}\right)\right]\exp(-jwt)\mathrm{d}t. \tag{11}$$

For the range bin at r, from the frequency shift between $\tilde{s}_1(w;r)$ and $\tilde{s}_2(w;r)$, the Doppler rate can be determined by the following equation:

$$\Delta w_r = a_r T_a = (a + b \cdot r)T_a \tag{12}$$

where Δw_r denotes the Doppler frequency shift corresponding to the range bin at r. Δw_r is estimated from the cross-correlation function of $|\tilde{s}_1(w;r)|$ and $|\tilde{s}_2(w;r)|$.

The cross-correlation function can be expressed by the following equation:

$$R_{\mathrm{MD}}(\eta;r) = \int_{-\frac{T_a}{4}}^{\frac{T_a}{4}} |\tilde{s}_1(w;r)| \cdot |\tilde{s}_2(w+\eta;r)|\mathrm{d}w \tag{13}$$

where η represents the horizontal axis of the cross-correlation function. The estimation of Doppler frequency shift Δw_r corresponds to the peak location of the cross-correlation function.

By straightforwardly non-coherent summation of the cross-correlation functions of some prominent range bins, the Doppler rate is ready to estimate accurately. In real data application of the MD algorithm, this non-coherent summation is promisingly significant to ensure the reliability and robustness. It suppresses the interference from some potential range bins, which would provide improper correlation functions with wrong peaks. Hence, direct summation in conventional MD algorithm is not suitable for the range-dependent cases.

3. Coherent RDMD algorithm

3.1 Principle of CRDMD algorithm

It is notable that, considering the range-dependence of the Doppler rate, the frequency shift linearly changes along the range bin. From (12), one can find that, frequency shift Δw_r corresponds to the peak location of the cross-correlation function at range r. According to the relationship mentioned above, the principle of CRDMD is derived in this subsection.

The coherent cross-correlation peaks of different range bins distribute along a slant line, whose slope corresponds to the range-dependence coefficient b similar to that in (5). The most significant difference between coherent and and non-coherent RDMD is the cross-correlation function. Compared with (13), the coherent cross-correlation function is modified by [19] as follows:

$$R_{\mathrm{CMD}}(\eta;r) =$$
$$\int_{-\frac{\mathrm{PRF}}{2}}^{\frac{\mathrm{PRF}}{2}} \left[\tilde{s}_1(w;r)\exp\left(-j\omega\frac{T_a}{2}\right)\right] \cdot \tilde{s}_2^*(w+\eta;r)\mathrm{d}w \tag{14}$$

where PRF is the pulse repeating frequency. Substituting (8) and (9) into (14), and ignoring the same convolution phase term $h(w)$, we can get an approximate equation given by

$$R_{\mathrm{CMD}}(\eta;r) \approx$$
$$\int_{-\frac{\mathrm{PRF}}{2}}^{\frac{\mathrm{PRF}}{2}} \bar{s}_{im}\left(w + \frac{a_r T_a}{2};r\right) \cdot \exp\left(-j\omega\frac{T_a}{4}\right) \cdot$$
$$\bar{s}_{im}^*\left(w + \eta - \frac{a_r T_a}{2};r\right) \cdot \exp\left(j(w+\eta)\frac{T_a}{4}\right)\mathrm{d}w =$$
$$\int_{-\frac{\mathrm{PRF}}{2}}^{\frac{\mathrm{PRF}}{2}} \bar{s}_{im}\left(w + \frac{a_r T_a}{2};r\right) \cdot \bar{s}_{im}^*\left(w + \eta - \frac{a_r T_a}{2};r\right)\mathrm{d}w \cdot$$
$$\exp\left(j\eta\frac{T_a}{4}\right). \tag{15}$$

According to (15), it can reach a correlation peak at $a_r T_a$, the phase of correlated function is $\exp(ja_r T_a^2/4)$. Hence, we can estimate the quadratic phase error parameter a_r by calculating the peak position of coherent corre-

lation function R_{CMD}. It can be found in (15) that coherent correlation function R_{CMD} is related to range r, thus the peak position η is given by

$$\eta(r) = (a + b \cdot r) T_a + \varepsilon \tag{16}$$

where ε denotes the error. According to the two-parameter linear regression theory, estimation of range-variant phase error parameters $\hat{a}$ and $\hat{b}$ are given by

$$\hat{a} = \frac{\bar{\eta}}{T_a} - \frac{\bar{r} \sum_{i=1}^{K} (\eta_i - \bar{\eta})(r_i - \bar{r})}{T_a \sum_{i=1}^{K} (r_i - \bar{r})^2}, \tag{17}$$

$$\hat{b} = \frac{\sum_{i=1}^{K} (\eta_i - \bar{\eta})(r_i - \bar{r})}{T_a \sum_{i=1}^{K} (r_i - \bar{r})^2}, \tag{18}$$

where K represents the number of samples, i represents the serial number of samples, $\bar{\eta}$ represents the mean value of η, and $\bar{r}$ represents the mean value of r. The residual range-variant phase error estimation can be obtained by the method illustrated above, and then the implementation process of the method is explained in detail as follows.

3.2 Flowchart of the proposed algorithm

In this subsection, a detailed description of the proposed range-variant quadratic phase error estimation algorithm is provided. At the beginning, a flowchart as shown in Fig. 2 is given to illustrate an example of complete process of SAR imaging, in which the proposed CRDMD algorithm is embedded. The flowchart is based on classical chirp scaling algorithm (CSA), which is shown on the left side. Range-variant phase correction is achieved by iteratively using the proposed CRDMD algorithm.
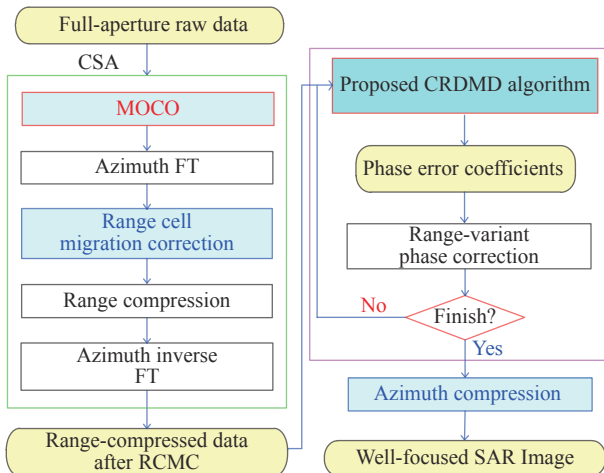

Fig. 2   An example of complete SAR imaging process

The left part of Fig. 2 is the conventional CSA processing, and the range and azimuth decoupling data result is finally obtained by MOCO, range cell migration correction (RCMC) and range compression. A "two-step" method can be used for MOCO to compensate the range variant and invariant parts of the motion errors. Due to the limitation of inertial navigation accuracy, the residual range variant phase error is still existing. The right part of Fig. 2 is the residual motion error estimation step. Coefficients of residual phase error can be estimated by CRDMD processing, then the range variant phase error is corrected by phase compensation. It should be noted that iterative processing is necessary, in order to ensure the convergence of the estimated phase error. The implementation of CRDMD is described in detail as follows.

The flowchart of the proposed CRDMD algorithm is given in Fig. 3. The main process can be divided into two stages: pre-processing stage and CRDMD core stage. In pre-processing stage, it mainly completes the input data sampling, initialization of the estimated parameter, and azimuth deramping. The CRDMD core stage is the critical part of the entire process, which contains the signal partition, coherent cross-correlation calculation, and parameter estimation.
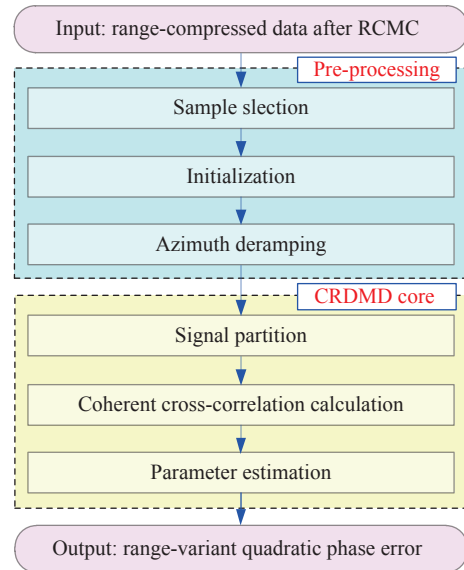

Fig. 3   Flowchart of the proposed CRDMD algorithm

Each of these steps above involves extensions, necessary step-by-step explanations are given below for better understanding.

(i) Input. The input of algorithm module is the signal after range cell migration correction. MOCO is carried out in the previous steps to compensate envelope and major phase errors caused by the non-stationary motion of the platform.

(ii) Sample selection. Strong scattering range bins for parameter estimation is selected due to the signal intensity. The selection of range bins needs to be relatively uniform in the range direction. Generally, we can first divide the whole range bins into N blocks, and then M range bins with strong reflection are selected in each range block. Therefore, the number of range bin samples used for estimation is $M \times N$.

(iii) Initialization. Range-variant Doppler rate coefficients a and b should be initialized. In the general case, the initial values of a and b are set to zero.

(iv) Azimuth deramping. Before the quadratic phase error estimation, it is necessary to compensate the known quadratic phase term by azimuth deramping; otherwise, the estimation of phase error will be affected. The quadratic phase term of (4) can be removed by multiplying an azimuth deramping function h related to azimuth time t and range r shown as follows:

$$h(t;r) = \exp\left[j\frac{4\pi}{\lambda}\sqrt{(vt-x)^2+r^2}\right] \cdot$$
$$\exp\left[-j\left(\hat{a}_0 + \hat{b}_0 \cdot r\right)t^2\right] \quad (19)$$

where $\hat{a}_0$ and $\hat{b}_0$ are estimated or initialized parameters during the previous operation.

(v) Signal partition. Echo signal is divided into two parts in azimuth so that sub-aperture signals $\tilde{s}_1(t;r)$ and $\tilde{s}_2(t;r)$ are obtained.

(vi) Coherent cross-correction calculation. The main purpose of coherent cross-correction calculation is to calculate the coherent correlation function R_{CMD}. Perform azimuth FT to $\tilde{s}_1(t;r)$ and $\tilde{s}_2(t;r)$, and the sub-aperture signals are transformed to the azimuth frequency domain, which is shown as $\tilde{s}_1(\omega;r)$ and $\tilde{s}_2(\omega;r)$. Then the coherent correlation function R_{CMD} can be calculated by (14).

(vii) Parameter estimation. For each signal sample $\tilde{s}(t;r)$ at range r, we can find the position $\eta(r)$ at peak value of $R_{\text{CMD}}(\eta;r)$, and then parameters a and b are estimated by a linear regression shown in (17) and (18).

(viii) Output. With fewer iterations, the estimated range-variant phase error is finally obtained.

3.3 Limitation discussion

Compared with RDMD, the proposed method provides a coherent integration for cross-coherent function calculation, which improves the estimation accuracy and also reduces the number of iterations required. As a negative price, the response curve of correlation function is more sensitive to signal phase error because of the coherent integration.

The main limitation of the proposed method is signal decoherence, which can be expressed as an error phase in the coherence integral in (14). The modified coherent cross-correlation function R'_{CMD} is given by

$$R'_{\text{CMD}}(\eta;r) =$$
$$\int_{-\frac{\text{PRF}}{2}}^{\frac{\text{PRF}}{2}} \left[\tilde{s}_1(w;r)\exp\left(-j\omega\frac{T_a}{2}\right)\right] \cdot \tilde{s}_2^*(w+\eta;r) \cdot$$
$$\exp\left[j\xi(\omega)\right]dw \quad (20)$$

where $\xi(\omega)$ represents the decoherence phase error generally induced by higher order terms of residual phase errors. When there are prominent third-order or higher-order phase error components in the echo data, the peak performance of coherent cross-correlation function will decline due to the unexpected decoherence phase error.

4. Real measured data experiments

4.1 X-band data experiment

The first real measured data experiment set is given in this subsection. The experimental radar system operates in X-band, which is equipped on an experimental UAV platform. The main system parameters are shown in Table 1.

Table 1 System parameters for Experiment 1

Parameter	Value
Working band	X-band
Resolution/m	0.75
Height/km	3
Speed/(m·s^{-1})	60
Slant range/km	13

A middle accuracy inertial measurement unit (IMU) with the Global Positioning System (GPS) is equipped on the radar system to measure the position and attitude information of radar platform. Due to the limited accuracy of the motion information, MOCO with IMU measurements is insufficient to generate the high quality imagery and therefore autofocus MOCO is necessary to overcome the residue motion error. Fig. 4 shows the the imaging results of a scene with various MOCO methods including the INS-only MOCO, conventional MD, RDMD, and the proposed CRDMD. In Fig. 4, the horizontal is the range direction, and the vertical is the azimuth direction. It can be found in Fig. 4(a) that the INS-only MOCO based imaging result is conspicuously blurred by residual phase errors due to the low accuracy of inertial navigation, which include the variant and invariant parts.

(a) MOCO with INS-only (X-band)

(b) MOCO with conventional MD (X-band)
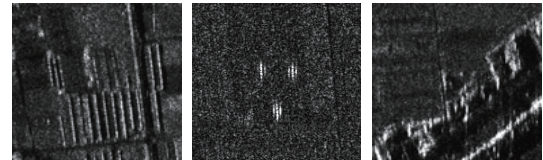

(c) MOCO with RDMD (X-band)

(d) MOCO with CRDMD (X-band)

Fig. 4   X-band UAV SAR images

In order to compare the performance of three autofocus methods in detail, reflector images in the scene are

extrated and shown in Fig. 5. It is shown in Fig. 5(a) that conventional MD cannot focus the reflectors well, because the space-variant phase error is non-negligible. Since the residual range-variant motion error is compensated, the imaging performance of the reflectors in Fig. 5(b) and Fig. 5(c) is significantly improved.

(a) MOCO with conventional MD (X-band)


(b) MOCO with RDMD (X-band)
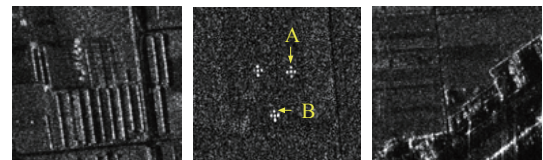
(c) MOCO with CRDMD (X-band)

Fig. 5   Magnified sub-scene images (X-band)

Two point-like targets are selected from Fig. 5(c), and their azimuth impulse response curves under the three autofocusing methods are analyzed respectively, which are shown in Fig. 6. Fig. 6 shows that the focusing performance of the target point under CRDMD is slightly better than RDMD, and significantly better than that under conventional MD. In this experiment, conventional MD and RDMD both use more than three iterations to realize convergence, while CRDMD only uses one iteration due to the phase coherent. In the case of the same focusing quality, the computing efficiency of CRDMD is significantly better than RDMD.

(a) Azimuth response of Point A

(b) Azimuth response of Point B

—— : CRDMD; —— : RDMD; ----- : Conventional MD.
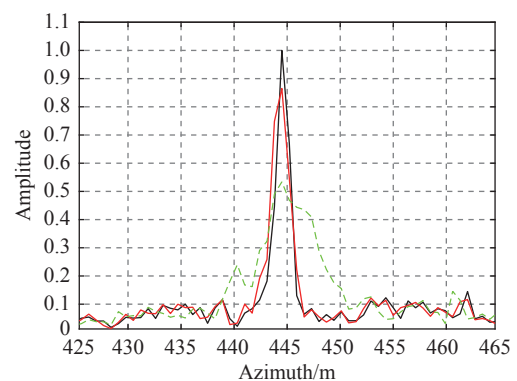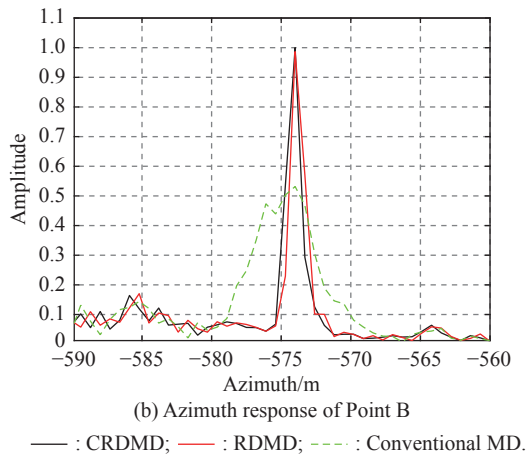
**Fig. 6   Azimuth impulse response curves of point-like targets (X-band)**

4.2   Ka-band data experiment

In order to verify the performance of the proposed method for imaging focusing in different working bands, a set of Ka-band image focusing experiments are presented in this subsection. The key system parameters of this experiment are shown in Table 2.

Table 2   System parameters for Experiment 2

| Parameter	Value
Working band	Ka-band
Resolution/m	0.3
Height/km	3
Speed/(m·s^{-1})	70
Slant range/km	10

Experiment is conducted in a desert area, and the experimental system is a Ka-band SAR loaded on UAV platform. Due to the high working frequency, the imaging quality is easily affected by residual phase error. Therefore, autofocusing is an indispensable MOCO method commonly used for real measured SAR data processing. Due to the lack of strong scattering points in the desert scene for PGA strategy, MD based autofocusing method is more applicable. Fig. 7 shows the imaging results of the experimental scene using conventional MD, RDMD and CRDMD methods respectively, where the horizontal is the range direction and the vertical is the azimuth direction.
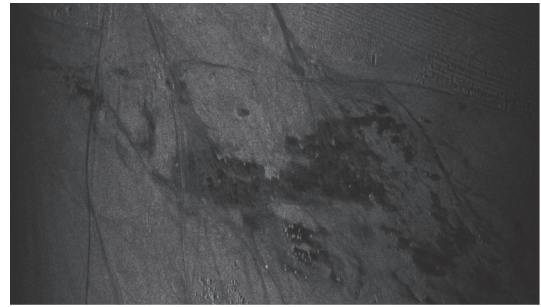
(a) MOCO with conventional MD (Ka-band)
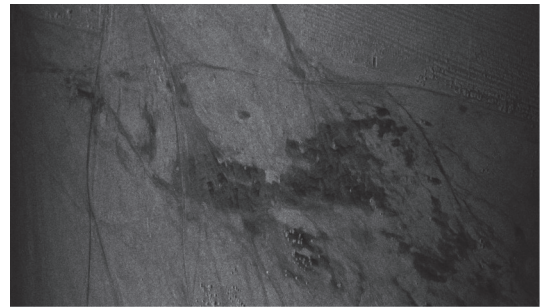
(b) MOCO with RDMD (Ka-band)
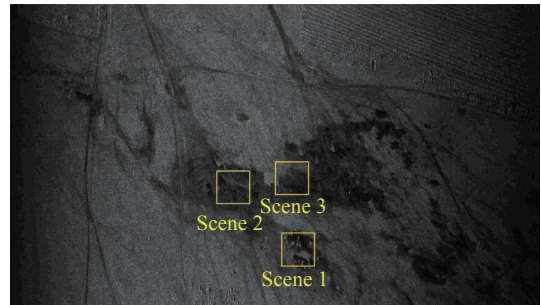
(c) MOCO with CRDMD (Ka-band)

Fig. 7   Ka-band UAV SAR images

Three sub-scenes are selected in Fig. 7, and the comparison results under the three autofocusing algorithms are shown in Fig. 8. In order to compare the focusing performance, two point like targets C and D are selected from Fig. 8, and the azimuth impulse response curves of the target points under the three autofocusing methods are respectively given in Fig. 9. Due to the relatively high phase sensitivity for Ka-band SAR imaging, the residual range-variant phase error of conventional MD algorithm has a significant influence on the focusing performance of the point-like targets. Due to the compensation of residual range-variant phase error, CRDMD and RDMD are both significantly better than conventional MD algorithms. Because of the sensitivity of phase coherent, the iteration time for CRDMD is only one, comparing with RDMD of three for convergence. As the result shown in Fig. 9, CRDMD has slightly better focusing performance than RDMD with fewer iterations.
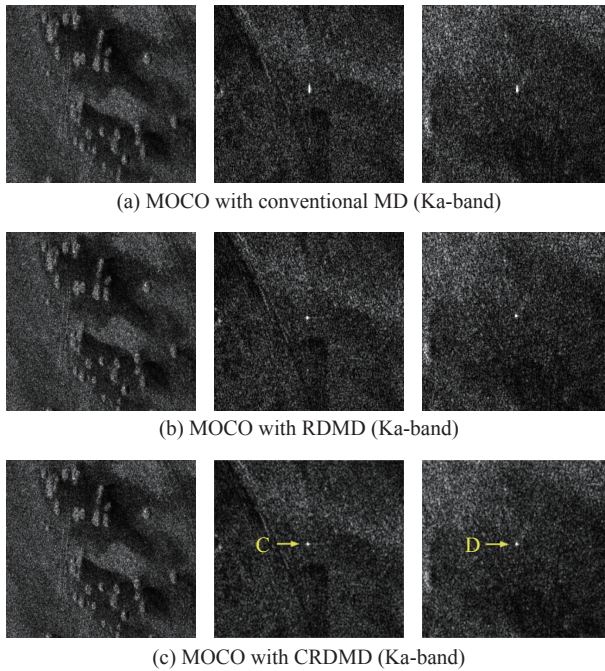
(a) MOCO with conventional MD (Ka-band)

(b) MOCO with RDMD (Ka-band)

(c) MOCO with CRDMD (Ka-band)

Fig. 8   Magnified sub-scene images (Ka-band)

(a) Azimuth response of Point C

(b) Azimuth response of Point D

——— : CRDMD;   ——— : RDMD;   - - - - : Conventional MD.
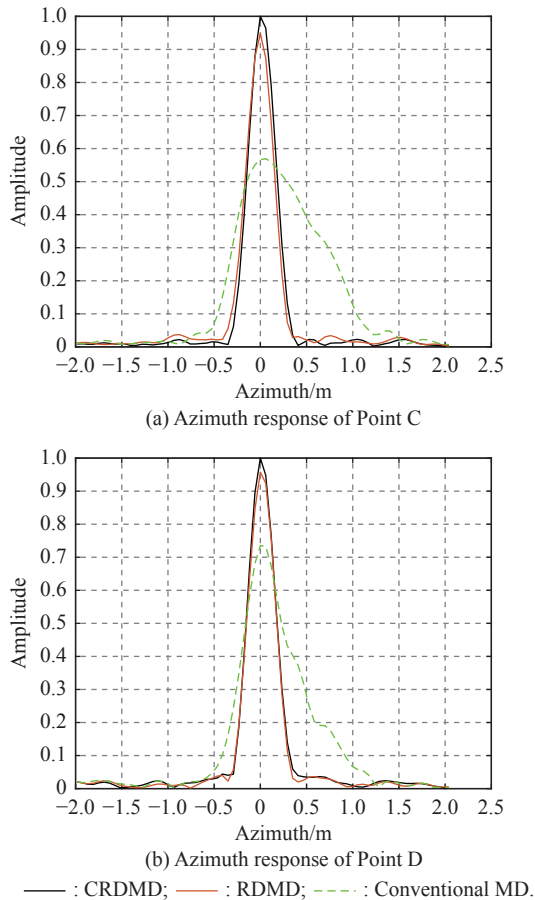
Fig. 9   Azimuth impulse response curves of point-like targets (Ka-band)

In addition, azimuth blocking strategy is adopted in the autofocusing processing of the X-band and Ka-band experiments, in which the azimuth block size is set to 256. Due to the fact that the proposed method is based on phase coherent MD, the correlation is superior to the amplitude correlation method under short apertures. It is suitable for sub-aperture autofocusing and has better performance to estimate the high-order phase error. Above experiments verify that the proposed CRDMD is more effective for residual range-variant motion error compensation in complex scenarios.

5. Conclusions

In this paper, a CRDMD algorithm is developed for airborne SAR image focusing. The sensitivity of the coherent correlation function provides a more accurate and efficient estimation for the residual range-variant phase errors. Real measured data experiments illustrate that the proposed CRDMD algorithm can achieve a more accurate and efficient range-variant phase error estimation comparing with conventional MD and RDMD algorithms. The limitation of this method is that it can only be used to estimate the variant motion error in range direction. In future work, we will study the coherent compensation method of two-dimensional variant motion error.

References

[1] CARRAR W G, GOODMAN R S, MAJEWSKI R M. Spotlight synthetic aperture radar: signal processing algorithm. Boston: Artech House, 1995.

[2] CUMMING I G, WONG F H. Digital processing of synthetic aperture radar data: algorithms and implementation. Norwood: Artech House, 2005.

[3] MOREIRA A, HUANG Y H. Airborne SAR processing of highly squinted data using a chirp scaling approach with integrated motion compensation. IEEE Trans. on Geoscience and Remote Sensing, 1994, 32(5): 1029–1040.

[4] LI Y K, LIU C, WANG Y F, et al. A robust motion error estimation method based on raw data. IEEE Trans. on Geoscience and Remote Sensing, 2012, 50(7): 2780–2790.

[5] YI T Z, HE Z H, HE F, et al. A compensation method for airborne SAR with varying accelerated motion error. Remote Sensing, 2018, 10(7): 1124.

[6] FAN B K, DING Z G, GAO W B, et al. An improved motion compensation method for high resolution UAV SAR. Science China Information Sciences, 2014, 57(12): 1–13.

[7] ZHANG L, QIAO Z J, YANG L, et al. A robust motion compensation approach for UAV SAR imagery. IEEE Trans. on Geoscience and Remote Sensing, 2012, 50(8): 3202–3218.

[8] GONZALEZ PARTIDA J T, ALMOROX GONZALEZ P, BURGOS GARCIA M. SAR system for UAV operation with motion error compensation beyond the resolution cell. Sensors, 2008, 8(5): 3384–3405.

[9] XU W D, WANG B N, XIANG M S, et al. A novel autofocus framework for UAV SAR imagery: motion error extraction from symmetric triangular FMCW differential signal. IEEE Trans. on Geoscience and Remote Sensing, 2022, 60: 5218915.

[10] ZHOU S, YANG L, ZHAO L F, et al. Quasi-polar-based FFBP algorithm for miniature UAV SAR imaging without navigational data. IEEE Trans. on Geoscience and Remote Sensing, 2017, 55(12): 7053–7065.

[11] XING M D, JIANG X W, WU R B, et al. Motion compensation for UAV SAR based on raw radar data. IEEE Trans. on Geoscience and Remote Sensing, 2009, 47(8): 2870–2883.

[12] LI Y K, YOUNG S O. Kalman filter disciplined phase gradient autofocus for stripmap SAR. IEEE Trans. on Geoscience and Remote Sensing, 2020, 58(9): 6298–6308.

[13] LIN H, CHEN J L, XING M D, et al. Time-domain autofocus for ultrahigh resolution SAR based on azimuth scaling transformation. IEEE Trans. on Geoscience and Remote Sensing, 2022, 60: 5227812.

[14] WAHL D E, EICHEL P H, GHIGLIA D C, et al. Phase gradient autofocus-a robust tool for high resolution SAR phase correction. IEEE Trans. on Aerospace and Electronic Systems, 1994, 30(3): 827–835.

[15] HUANG Y, LIU F Y, CHEN Z Y, et al. An improved map-drift algorithm for unmanned aerial vehicle SAR imaging. IEEE Geoscience and Remote Sensing Letters, 2021, 18(11): 1–5.

[16] CHEN J L, XING M D, YU H W, et al. Motion compensation autofocus in airborne synthetic aperture radar: a review. IEEE Geoscience and Remote Sensing Magazine, 2022, 10(1): 185−206.

[17] CHEN J L, LIANG B G, ZHANG J C, et al. Efficiency and robustness improvement of airborne SAR motion compensation with high resolution and wide swath. IEEE Geoscience and Remote Sensing Letters, 2022, 19: 4004005.

[18] DING Z G, LI L H, WANG Y, et al. An autofocus approach for UAV-based ultrawideband ultrawidebeam SAR data with frequency-dependent and 2-D space-variant motion errors. IEEE Trans. on Geoscience and Remote Sensing, 2022, 60: 5203518.

[19] WANG G Y, ZHANG M, HUANG Y, et al. Robust two-dimensional spatial-variant map-drift algorithm for UAV SAR autofocusing. Remote Sensing, 2019, 11(3): 340.

[20] MENG Z C, ZHANG L, LI J, et al. Time-domain azimuth-variant MOCO algorithm for airborne SAR imaging. IEEE Geoscience and Remote Sensing Letters, 2022, 19: 4508605.

[21] PRATS P, REIGBER A, MALLORQUI J J. Topography-dependent motion compensation for repeat-pass interferometric SAR systems. IEEE Geoscience and Remote Sensing Letters, 2005, 2(2): 206–210.

[22] ZHANG L, WANG G Y, QIAO Z J, et al. Azimuth motion compensation with improved subaperture algorithm for airborne SAR imaging. IEEE Journal of Selected Topics in Applied Earth Observations and Remote Sensing, 2017, 10(1): 184–193.

[23] CHEN X X, WAN M H, XING M D, et al. Azimuth variant motion error compensation algorithm for airborne SAR imaging based on Doppler adjustment. IEEE Geoscience and Remote Sensing Letters, 2022, 19: 4010305.

[24] REN Y, TANG S Y, GUO P, et al. 2-D spatially variant motion error compensation for high-resolution airborne SAR based on range-doppler expansion approach. IEEE Trans. on Geoscience and Remote Sensing, 2022, 60: 5201413.

[25] LU J Y, ZHANG L, QUAN Y H, et al. Parametric azimuth-variant motion compensation for forward-looking multichannel SAR imagery. IEEE Trans. on Geoscience and Remote Sensing, 2021, 59(10): 8521–8537.

[26] LU Q R, GAO Y S, HUANG P H, et al. Range- and aperture-dependent motion compensation based on precise frequency division and chirp scaling for synthetic aperture radar. IEEE Sensors Journal, 2019, 19(4): 1435–1442.

[27] YANG M D, ZHU D Y. Efficient space-variant motion compensation approach for ultra-high-resolution SAR based on subswath processing. IEEE Journal of Selected Topics in Applied Earth Observations and Remote Sensing, 2018, 11(6): 2090–2103.

[28] ZHANG L, HU M Q, WANG G Y, et al. Range-dependent map-drift algorithm for focusing UAV SAR imagery. IEEE Geoscience and Remote Sensing Letters, 2016, 13(8): 1158–1162.

[29] SAMCZYNSKI P, KULPA K S. Coherent mapdrift technique. IEEE Trans. on Geoscience and Remote Sensing, 2010, 48(3): 1505–1517.

[30] SAMCZYNSKI P. Super convergent velocity estimator for an autofocus coherent mapdrift technique. IEEE Trans. on Geoscience and Remote Sensing, 2012, 9(2): 204–208.

[31] ZHANG L, SHENG J L, XING M D, et al. Wavenumber-domain autofocusing for highly squinted UAV SAR imagery. IEEE Sensors Journal, 2012, 12(5): 1574–1588.

Biographies

ZHANG Man was born in 1984. She received her Ph.D. degree from Xidian Univeristy. She is a lecturer in Guangzhou University. Her research interests are radar signal processing and machine learning in radar imaging.
E-mail: manzhang401@gzhu.edu.cn

WANG Guanyong was born in 1989. He received his B.S. degree from Tianjin University in 2011, and M.S. and Ph.D. degrees from the Defence Technology Academy of China Aerospace Science and Industry Corporation in 2014 and 2018. He is a senior engineer in Beijing Institute of Radio Measurement. His research interests are high band synthetic aperture radar (SAR) imaging and high precision motion compensation technology, such as millimeter wave SAR signal processing.
E-mail: guanbingwang@126.com

WEI Feiming was born in 1983. He received his M.S. degree from University of Electronic Science and Technology of China. He is a professor in No.802 Research Institute of Shanghai Academy of Spaceflight Technology, and a doctor of engineering in Shanghai Jiao Tong University. His research interests are radar target detection and recognition.
E-mail: weifeiming@sjtu.edu.cn

JIN Xue was born in 1988. She received her M.S. degree from Beijing Institute of Technology in 2013. She is a research associate in Beijing Institute of Tracking and Communication Technology. Her research interest is image processing.
E-mail: cara_snow@163.com